References

BACOVA, M., ZELINKOVA, E. & ZELINKA, J. (1971). *Biochim. Biophys. Acta*, **235**, 335–338.
BLOW, D. M. & CRICK, F. H. (1959). *Acta Cryst.* **12**, 794–802.
BOTH, V., ZACHAR, J. & ZELINKA, J. (1983). *Gen. Physiol. Biophys.* **2**, 269–278.
DODSON, E. J. (1975). *Crystallographic Computing Techniques*, edited by F. R. AHMED, pp. 259–268. Copenhagen: Munksgaard.
EVANS, P. R. (1987). *Computational Aspects of Protein Crystal Data Analysis. Proceedings of the Daresbury Study Weekend*, edited by J. R. HELLIWELL, P. R. MACHIN & M. Z. PAPIZ, pp. 58–65. Daresbury, UK: Science and Engineering Research Council.
FINDLAY, D., HERRIES, D. G., MATHIAS, A. P., RANBIN, B. R. & ROSS, C. A. (1961). *Nature (London)*, **190**, 781–784.
GASPERIK, J., PRESCAKOVA, S. & ZELINKA, J. (1982). *Biologia*, **36**, 377–381.
HENDRICKSON, W. A. (1985). *Methods Enzymol.* **115**, 252–270.
HENDRICKSON, W. A. & KONNERT, J. H. (1980). *Computing in Crystallography*, edited by R. DIAMOND, S. RAMASESHAN & K. VENKATESAN, pp. 1310–1323. Bangalore: Indian Academy of Sciences.
HILL, C. P., DODSON, G. G., HEINEMANN, U., SAENGER, W., MITSUI, Y., NAKAMURA, K., BORISOV, S., TISCHENKO, G., POLYAKOV, K. & PAVLOVSKY, S. (1983). *TIBS*, **8**, 364–369.
IKEHARA, M., OHTSUKA, E., TOKUNAGA, T., NISHIKAWA, S., UESIGI, S., TANAKA, T., AOYAMA, Y., KIKYODANI, S., FUKIMOTO, K., YAMASE, K. FUCHIMURA, K. & MORIOKA, H. (1986). *Proc. Natl Acad. Sci. USA*, **83**, 4695–4699.
JONES, T. A. (1978). *J. Appl. Cryst.* **11**, 268–272.
LUZZATI, V. (1952). *Acta Cryst.* **5**, 802–810.
NISHIKAWA, S., MORIOKA, H., KIM, H., FUCHIMURA, K., TANAKA, T., UESUGI, S., HAKOSHIMA, T., TOMITA, K., OHTSUKA, E. & IKEHARA, M. (1987). *Biochemistry*, **26**, 8620–8624.
NORTH, A. C. T., PHILLIPS, D. C. & MATHEWS, F. S. (1968). *Acta Cryst.* A**24**, 351–359.
SANISHVILI, R. G. (1988). Personal communication.
SEVCIK, J., GASPERIK, J. & ZELINKA, J. (1982). *Gen. Physiol. Biophys.* **1**, 255–259.
SHLYAPNIKOV, S. U., BOTH, V., KULIKOV, V. A., DEMENTIEV, A. A., SEVCIK, J. & ZELINKA, J. (1986). *FEBS Lett.* **209**, 335–339.
TAKAHASHI, K. (1970). *J. Biochem. (Tokyo)*, **67**, 833–839.
TAKAHASHI, K. & MOORE, S. (1982). *The Enzymes*, 3rd ed., Vol. 15, *Nucleic Acids*, Part B, pp. 435–467. New York: Academic Press.
VIJAYAN, M. (1980). *Acta Cryst.* A**36**, 215–310.
WANG, B. C. (1985). *Methods Enzymol.* **114**, 90–112.
WILSON, K. S. (1978). *Acta Cryst.* B**34**, 1599–1608.
WINKLER, F. K., SCHUTT, C. E. & HARRISON, S. C. (1979). *Acta Cryst.* A**35**, 901–911.
ZELINKOVA, E., BACOVA, M. & ZELINKA, J. (1971). *Biochim. Biophys. Acta*, **235**, 343–344.

Acta Cryst. (1991). B**47**, 253–266

Electron Distributions in Peptides and Related Molecules. 1. An Experimental and Theoretical Study of *N*-Acetyl-L-tryptophan Methylamide

BY MOHAMED SOUHASSOU, CLAUDE LECOMTE,* ROBERT H. BLESSING† AND ANDRÉ AUBRY

Laboratoire de Minéralogie et Cristallographie, URA CNRS 809, *Université de Nancy* I, *Faculté des Sciences, BP* 239, 54506 *Vandoeuvre les Nancy CEDEX, France*

MARIE-MADELEINE ROHMER, ROLAND WIEST AND MARC BÉNARD

Laboratoire de Chimie Quantique, ER 139 *au CNRS, Université Louis Pasteur*, 4 *rue Blaise Pascal*, 67000 *Strasbourg, France*

AND MICHEL MARRAUD

Laboratoire de Chimie Physique Macromoléculaire, URA CNRS 494, *ENSIC INPL, BP* 451, 54001 *Nancy CEDEX, France*

(*Received* 19 *January* 1990; *accepted* 24 *September* 1990)

Abstract

The thermal vibrations and electron density of *N*-Ac-L-Trp-NHMe have been analyzed using single-crystal X-ray diffraction data measured at 103 K with Mo $K\alpha$ radiation to a resolution corresponding to $(\sin\theta_{max})/\lambda = 1{\cdot}17$ Å^{-1}. Measurements of 10 527 reflections gave 4913 unique data [$R_{int}(|F|^2) = 0{\cdot}019$] of which 2641 had $I > 3\sigma(I)$. A multipolar atomic density model was fitted [$R(|F|) = 0{\cdot}028$] in order to calculate phases for the crystal structure factors and map the valence-electron distribution. The phase problem for determining deformation densities by Fourier synthesis for noncentrosymmetric crystals is discussed. The experimental density agrees well with the theoretical density from an *ab initio* SCF molecular wave function calculated at the

* Author to whom correspondence should be addressed.
† Permanent address: Medical Foundation of Buffalo, 73 High Street, Buffalo, New York 14203, USA.

0108-7681/91/020253-14$03.00

crystallographic molecular geometry with a split-valence basis set. Both the experimental and theoretical analyses confirm that the electron distribution is the same in the two different peptide groups in the molecule. Crystal data: $C_{14}H_{17}N_3O_2$, $M_r = 259{\cdot}31$, orthorhombic, $P2_12_12_1$, $Z = 4$, $F(000) = 522$ e from 295 to 103 K; at 295 K, $a = 8{\cdot}152$ (2), $b = 11{\cdot}170$ (2), $c = 15{\cdot}068$ (3) Å, $V = 1372$ Å^3, $D_x = 1{\cdot}26$ mg mm^{-3}; at 103 K, $a = 8{\cdot}209$ (3), $b = 11{\cdot}016$ (2), $c = 14{\cdot}760$ (4) Å, $V = 1335$ Å^3, $D_x = 1{\cdot}29$ mg mm^{-3}, $\mu = 0{\cdot}083$ mm^{-1} for $\lambda = 0{\cdot}7107$ Å.

Introduction

Most molecular biological processes are initiated by a preliminary step in which two molecular species recognize each other and form a complex. Among the forces stabilizing molecular complexes, electrostatic interactions between stereochemically complementary charge distributions are probably the most important. Because the electrostatic potential falls off with distance as r^{-1}, electrostatic intermolecular interactions have a longer range than van der Waals interactions, for which the attractive term in the potential falls off as r^{-6} and quickly becomes negligible at moderate interaction distances.

Electrostatic intermolecular interactions have often been analyzed by modelling molecules as constellations of point charges. This approach can be useful at large interaction distances, but it is a very rough approximation at short distances. Accurate electrostatic potentials for the nuclear and electronic molecular charge distributions permit analysis down to very short contact distances, within which polarization and exchange phenomena begin to be significant.

The present paper reports the first in a series of studies of the charge-density distributions in peptides. Experimental and theoretical electron densities are compared for an example of the simplest protein subunit, a single amino-acid residue – tryptophan in the present case – protected by an amide function at both its amino and carboxyl ends (see scheme below).

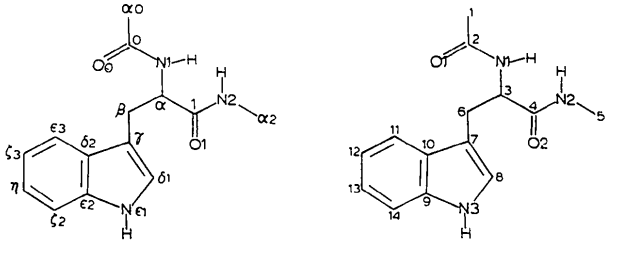

IUPAC and 'working' atom labels

Cα0	C1	C1	C4	Cγ	C7	Cε3	C11
C0	C2	O1	O2	Cδ1	C8	Cζ2	C14
O0	O1	N2	N2	Cδ2	C10	Cζ3	C12
N1	N1	Cα2	C5	Nε1	N3	Cη	C13
Cα	C3	Cβ	C6	Cε2	C9		

Experimental

N-Ac-L-Trp-NHMe was synthesized by treatment of the ester (Biochem. E-1230) with methylamine in absolute ethanol, and recrystallized from ethanol–ethyl acetate by solvent evaporation. A crystal 0·45 × 0·30 × 0·35 mm was used to measure Mo $K\alpha$ X-ray diffraction data on an Enraf–Nonius CAD-4 diffractometer equipped with a liquid nitrogen vapor-stream low-temperature apparatus and installed in a dry box to prevent ice formation on the crystal. The gas-stream temperature was maintained at 103 ± 5 K as monitored by a copper–constantan thermocouple positioned ~5 cm upstream from the crystal. The homogeneity of the beam from the graphite incident-beam monochromator was measured, and the intensity varied by less than 3·5% over the area intercepted by the specimen crystal. Lattice parameters were obtained by least-squares fit to the optimized setting angles of the $K\alpha_1$ peaks of 24 reflections with $28 < 2\theta < 38°$. As shown in the *Abstract*, one unit-cell edge was found to increase with decreasing temperature (from $a = 8{\cdot}150$ Å at 295 K to 8·209 Å at 103 K), but the unit-cell volume did decrease with temperature, and no change in crystal symmetry was detected. There was, however, a noticeable increase in the mosaic spread, and this might be related to the eventual spontaneous fracture of the crystal before the planned data collection was entirely completed.

Intensity data were recorded as $\omega/2\theta$ scan profiles to a resolution of $s = (\sin\theta)/\lambda = 1{\cdot}17$ Å^{-1} for a total of 10 527 reflections in at least two symmetry-equivalent octants in the following way: for reflections with $s < 0{\cdot}5$ Å^{-1} four equivalents, and with $0{\cdot}5 < s < 0{\cdot}9$ Å^{-1} two equivalents, were measured. After a conventional refinement against these low-angle data, high-angle data were calculated to $s = 1{\cdot}2$ Å^{-1}, and for those with an estimated $I > 4\sigma(I)$ two equivalents were measured. The measurements were stopped because the crystal fractured, and it was judged unnecessary to attempt to measure the remaining 100 to 200 significant reflections with a second crystal. During the data collection six standard reflections, 555, $\bar{5}55$, 600, $\bar{6}00$, 014 and 213, were measured at 4 h intervals.

Data reduction and error analysis were carried out using the programs of Blessing (1989). Reflection integration limits were taken from a Lorentzian model for peak-width variations. A polynomial fit to the smooth decline of ~1·2% in the standard-reflection intensities over the ~400 h of X-ray exposure was used to scale the data, and to derive a proportional error coefficient, $p = 0{\cdot}019$, for the calculation of $\sigma^2(|F|^2) = \sigma_c^2 + (p|F|^2)^2$ with σ_c from propagation-of-error calculations in which counting statistics and scan-angle setting uncertainties [$\sigma(\omega) =$

0·005°] made the most important contributions. The rather large value of p is probably mainly due to the ±5 K instabilities of the low-temperature apparatus. Absorption and beam-inhomogeneity corrections were deemed unnecessary. Averaging equivalent measurements gave 4913 unique data, of which 2641 had $I > 3\sigma(I)$. The internal-agreement indices, defined as $R = \sum||F|^2 - \langle|F|\rangle^2|/\sum|F|^2$ and $wR = [\sum w(|F|^2 - \langle|F|^2\rangle)^2/\sum w(|F|^2)^2]^{1/2}$, $w = 1/\sigma^2(|F|^2)$, were $R = 0{\cdot}019$ and $wR = 0{\cdot}052$ for all data, and 0·017 and 0·028 for the 837 data with $s < 0{\cdot}5$ Å^{-1}.

Crystallographic analysis

The crystal structure was known from a preliminary room-temperature study (Souhassou, Aubry, Lecomte & Marraud, 1990).

Least-squares refinements

Since there were only 650 data with $s = (\sin\theta)/\lambda > 0{\cdot}9$ Å^{-1} and $q = I/\sigma(I) > 3$, a high-angle refinement of the non-H atoms was made against the 1511 data with $s > 0{\cdot}6$ Å^{-1} and $q > 3$. Statistics of fit are given in Table 1. H atoms were found by difference Fourier synthesis ($s < 0{\cdot}9$ Å^{-1}) and refined isotropically, after which their coordinates were adjusted by extending along the C—H and N—H bond directions to bond lengths of 1·07 Å (C—H) and 1·03 Å (N—H), equal to average values from neutron diffraction (Allen, 1986). The bound-atom form factor for hydrogen was taken from Stewart, Davidson & Simpson (1965), and the form factors for the non-H atoms were as calculated from Clementi & Raimondi (1963) free-atom wave functions. The real and imaginary anomalous-dispersion corrections to the form factors given by Cromer (1974) were included in the structure-factor least-squares calculations, but they were removed from the structure factors used for the Fourier mapping of the electron density.

Because the structure is noncentrosymmetric, it is necessary to have very accurate phases for the structure factors in order to get reliable electron density maps. The necessary accuracy can be attained using a multipolar atomic electron density model. In the model used in the present work (Hansen & Coppens, 1978), electron densities at each atom are described by

$$\rho(\mathbf{r}) = \rho_c(r) + P_v\kappa^3\rho_v(\kappa r) + \sum_{l=0}^{3}\kappa'^3 R_l(\kappa' r) \times \sum_{m=-l}^{+l} P_{lm}y_{lm}(\theta,\varphi) \quad (1)$$

where ρ_c and ρ_v are spherically averaged Hartree–Fock core and valence densities, with the ρ_v normalized to one electron, the y_{lm} are the multipolar spherical harmonic angular functions in real form, and the $R_l = N_l r^n \exp(-\kappa'\zeta r)$ are Slater-type radial functions, in which N_l is a normalization factor, and $n = n(l)$ and ζ are parameters chosen according to the criteria given by Hansen & Coppens (1978). The refinable parameters are the valence-shell contraction–expansion parameters κ and κ' and the population parameters P_v and P_{lm}. The limit $l_{max} = 3$ corresponds to truncation of the multipole expansion at the octupole level for the non-H atoms.

Table 1. *Least-squares refinement statistics of fit*

$\chi^2 = \sum w(|F_o| - k|F_c|)^2$, $w = 1/\sigma^2(|F_o|)$, $w = 0$ if $I < 3\sigma(I)$; $R = \sum||F_o| - k|F_c||/\sum|F_o|$; $wR = (\chi^2/\sum w|F_o|^2)^{1/2}$; $S = [\chi^2/(n-m)]^{1/2}$, n data and m parameters. The values of $S < 1$ indicate a slight overestimation of the experimental errors, as explained in *Appendix A*. For the high-angle refinement, $(\sin\theta)/\lambda > 0{\cdot}6$ Å^{-1}. For the all-data refinement, isotropic H atoms varied; k and non-H atoms fixed from the high-angle refinement.

Refinement	R	wR	S	k	n	m
Spherical atoms						
High-angle data	0·0497	0·0477	0·82	0·4860 (2)	1511	173
All data	0·0529	0·0639	1·80	0·4680	2641	68
Multipolar atoms	0·0284	0·0236	0·77	0·4815 (2)	2641	465

To reduce the number of variables, chemical constraints were imposed on the multipole density parameters so that O0 = O1, N1 = N2, Cα0 = Cα2, C0 = C1, and Cε3 = Cζ2 = Cζ3 = Cη. Two types of H atoms were defined, H(C) and H(N), each with a monopole ($l = 0$) and a single dipole ($l = 1$, $m = 0$) along the H—C or H—N bond. The multipolar density parameters were initially refined with the structural parameters fixed at the values from the spherical-atom refinements, and then all the parameters were refined together. The valence-shell population parameters were constrained as described by Coppens (1977) to give an electrically neutral unit cell.

One difficulty was a slight instability of the scale factor, which varied from 0·4680 (3) after the high-angle spherical-atom refinement to 0·4970 (2) after the first multipole refinement. These scale factors left significant residual difference densities at the atomic positions; positive after the former refinement, and negative after the latter. Consequently, a new multipole refinement was performed with the scale factor initially fixed at 0·48 until convergence, and then finally allowed to vary along with all the other parameters. This procedure led to much smaller residual densities and gave the best statistics of fit (Table 1 and *Appendix A*). An extinction parameter was included in the early refinement cycles, but it did not refine to a significantly non-zero value, and it was therefore omitted from the final cycles.

Fig. 1 shows the final residual density map for the Cβ-indole group, which is planar to within 0·01 Å. The unfitted density presumably reflects residual scale-factor bias and an imperfect deconvolution of the thermal motion; it might also be partly attributable to the local chemical symmetry constraints

imposed in the multipole refinements. Estimates (Cruickshank, 1949) of the average error in the experimental difference-density maps are

$$\langle\sigma^2(\Delta\rho)\rangle^{1/2} \simeq V^{-1}k^{-1}[\sum_{\mathbf{h}}\sigma^2(|F_o|)]^{1/2} = 0{\cdot}06 \text{ e Å}^{-3} \quad (2a)$$

and

$$\langle\sigma^2(\Delta\rho)\rangle^{1/2} \simeq V^{-1}[\sum_{\mathbf{h}}(k^{-1}|F_o| - |F_m|)^2]^{1/2} = 0{\cdot}09 \text{ e Å}^{-3} \quad (2b)$$

where the subscript m designates the multipole model.

Final parameters are given in Tables 2, 3 and 4.* Fig. 2 shows the local orthogonal axes used in Table 4, Fig. 3 shows the molecular structure, and Fig. 4 the hydrogen bonding and crystal packing. Selected valence and conformation angles are given in Table 5; bond lengths are included in Table 7.

Thermal-vibration analysis

The rigid-bond test (Hirshfeld, 1976) indicated that the multipole refinement yielded a reasonably effective deconvolution of the mean-square atomic displacements from the valence-electron density deformations. The differences between mean-square displacements along interatomic directions had magnitudes $|\Delta| \leq 0{\cdot}001$ Å^2 for nearly all the bonded

* Tables of structure factors and residual-density maps for the peptide groups have been deposited with the British Library Document Supply Centre as Supplementary Publication No. SUP 53552 (13 pp.). Copies may be obtained through The Technical Editor, International Union of Crystallography, 5 Abbey Square, Chester CH1 2HU, England.

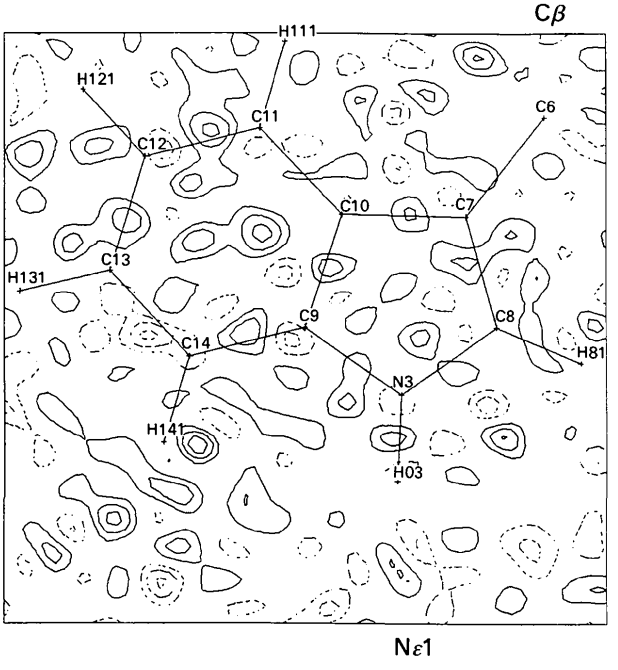

Fig. 1. Residual density, $\Delta\rho(\mathbf{r}) = v^{-1}\sum_{\mathbf{h}}(k^{-1}|F_o| - |F_m|)\exp(i\varphi_m) \times \exp(-2\pi i\mathbf{h}.\mathbf{r})$, in the plane of the Cβ-indole group. Contour interval 0·05 e Å^{-3}; positive contours solid, negative dashed; zero contour omitted for all experimental maps, but represented as a solid line for all quantum-chemical maps.

Table 2. *Final structure parameters (both IUPAC and 'working' atom labels are listed)*

For the non-H atoms, $U_{iso} = \sum_{i=1}^{3}[U^{ii}/\sigma^2(U^{ii})]/\sum_{i=1}^{3}[1/\sigma^2(U^{ii})]$.

H-atom positions were adjusted to give C—H and N—H bond lengths equal to average values from neutron diffraction.

		x	*y*	*z*	U_{iso} (Å^2)
Cα0	C1	−0·05536 (18)	−0·02161 (11)	0·44693 (9)	0·0204 (9)
C0	C2	−0·02695 (13)	0·08577 (9)	0·38687 (7)	0·0112 (6)
O0	O1	0·07040 (9)	0·08145 (7)	0·32205 (5)	0·0131 (5)
N1	N1	−0·11249 (11)	0·18577 (8)	0·40503 (6)	0·0120 (5)
Cα	C3	−0·09476 (13)	0·29475 (9)	0·35108 (7)	0·0111 (6)
C1	C4	0·06185 (13)	0·36363 (9)	0·37699 (7)	0·0115 (6)
O1	O2	0·14432 (10)	0·33608 (7)	0·44366 (5)	0·0149 (5)
N2	N2	0·10012 (12)	0·45301 (8)	0·31943 (7)	0·0164 (6)
Cα2	C5	0·24848 (15)	0·52394 (11)	0·32622 (9)	0·0184 (8)
Cβ	C6	−0·24963 (14)	0·37210 (10)	0·36040 (8)	0·0143 (7)
Cγ	C7	−0·39408 (13)	0·31289 (9)	0·31689 (7)	0·0123 (6)
Cδ1	C8	−0·50694 (13)	0·24010 (10)	0·35816 (8)	0·0155 (7)
Cδ2	C10	−0·43873 (13)	0·31791 (9)	0·22263 (7)	0·0118 (6)
Nε1	N3	−0·61895 (12)	0·19929 (9)	0·29611 (6)	0·0164 (6)
Cε2	C9	−0·58063 (13)	0·24643 (9)	0·21281 (7)	0·0126 (6)
Cε3	C11	−0·37390 (15)	0·37683 (10)	0·14626 (8)	0·0166 (7)
Cζ2	C14	−0·65878 (15)	0·23233 (10)	0·12931 (8)	0·0174 (8)
Cζ3	C12	−0·45145 (17)	0·36288 (11)	0·06370 (8)	0·0200 (8)
Cη	C13	−0·59278 (16)	0·29096 (10)	0·05534 (8)	0·0193 (8)
Hα01	H11	0·05668	−0·03183	0·48319	0·071 (7)
Hα02	H12	−0·06496	−0·10134	0·40587	0·049 (5)
Hα03	H13	−0·15933	−0·01029	0·48982	0·053 (5)
HN1	H01	−0·19851	0·18439	0·45582	0·022 (4)
Hα	H31	−0·07828	0·27182	0·28124	0·015 (3)
HN2	H02	0·02080	0·47618	0·26820	0·019 (4)
Hα21	H51	0·27154	0·56078	0·26038	0·033 (4)
Hα22	H52	0·22856	0·59526	0·37417	0·034 (4)
Hα23	H53	0·34970	0·46742	0·34373	0·021 (4)
Hβ1	H61	−0·22560	0·45918	0·33119	0·021 (4)
Hβ2	H62	−0·27365	0·38532	0·43096	0·018 (4)
Hδ1	H81	−0·51297	0·21337	0·42777	0·022 (4)
Hε1	H03	−0·72430	0·15118	0·30824	0·010 (4)
Hε3	H111	−0·26299	0·42745	0·15107	0·023 (4)
Hζ2	H141	−0·76759	0·17939	0·12365	0·023 (4)
Hζ3	H121	−0·39992	0·40812	0·00631	0·030 (4)
Hη	H131	−0·65078	0·27983	0·00905	0·031 (4)

Table 3. *Anisotropic mean-square atomic displacement parameters (Å^2) for the non-H atoms (both IUPAC and 'working' atom labels are listed)*

$$F(T) = F(0)\exp(-2\pi^2\sum_{i=1}^{3}\sum_{j=1}^{3}h_ih_ja^{*i}a^{*j}U^{ij}).$$

		U^{11}	U^{22}	U^{33}	U^{12}	U^{13}	U^{23}
Cα0	C1	0·0230 (9)	0·0147 (7)	0·0277 (9)	−0·0002 (7)	0·0066 (8)	0·0055 (6)
C0	C2	0·0103 (6)	0·0100 (6)	0·0137 (7)	−0·0007 (5)	0·0020 (5)	−0·0008 (6)
O0	O1	0·0110 (5)	0·0132 (4)	0·0150 (5)	−0·0004 (4)	0·0034 (4)	−0·0022 (4)
N1	N1	0·0113 (5)	0·0115 (5)	0·0131 (5)	0·0010 (5)	0·0035 (5)	0·0009 (4)
Cα	C3	0·0095 (6)	0·0117 (6)	0·0117 (5)	0·0013 (5)	−0·0002 (5)	−0·0002 (5)
C1	C4	0·0100 (6)	0·0126 (6)	0·0116 (6)	−0·0001 (5)	−0·0012 (6)	0·0012 (5)
O1	O2	0·0134 (5)	0·0196 (5)	0·0121 (5)	−0·0033 (5)	−0·0042 (5)	0·0034 (4)
N2	N2	0·0125 (6)	0·0188 (6)	0·0176 (6)	−0·0040 (5)	−0·0038 (6)	0·0076 (5)
Cα2	C5	0·0164 (8)	0·0169 (7)	0·0227 (8)	−0·0046 (7)	−0·0011 (7)	0·0040 (7)
Cβ	C6	0·0105 (7)	0·0137 (6)	0·0195 (7)	0·0020 (6)	−0·0031 (6)	−0·0046 (6)
Cγ	C7	0·0085 (6)	0·0152 (6)	0·0134 (6)	0·0001 (5)	−0·0021 (6)	0·0004 (5)
Cδ1	C8	0·0124 (7)	0·0216 (7)	0·0136 (7)	−0·0016 (6)	−0·0002 (6)	0·0020 (6)
Cδ2	C10	0·0093 (6)	0·0122 (6)	0·0142 (6)	0·0001 (5)	0·0003 (5)	0·0003 (5)
Nε1	N3	0·0110 (6)	0·0215 (6)	0·0171 (6)	−0·0046 (5)	0·0000 (5)	0·0042 (5)
Cε2	C9	0·0092 (6)	0·0141 (6)	0·0142 (6)	−0·0007 (6)	−0·0006 (6)	0·0006 (5)
Cε3	C11	0·0161 (7)	0·0172 (6)	0·0165 (7)	−0·0007 (6)	0·0036 (6)	0·0018 (6)
Cζ2	C14	0·0165 (7)	0·0176 (7)	0·0180 (8)	−0·0002 (6)	−0·0057 (7)	−0·0022 (6)
Cζ3	C12	0·0261 (9)	0·0220 (7)	0·0144 (7)	0·0026 (7)	0·0037 (7)	0·0027 (6)
Cη	C13	0·0243 (9)	0·0218 (8)	0·0147 (7)	0·0048 (8)	−0·0045 (7)	−0·0018 (6)

Table 4. *Multipolar atomic electron density parameters*

See Fig. 2 for the directions of local orthonormal reference axes for the atom-centered multipole functions. *PV*, valence-shell population; *D*, dipoles, $l = 1$; *Q*, quadrupoles, $l = 2$; *O*, octupoles, $l = 3$; κ, contraction–expansion parameter for the spherical valence-shell density; κ', contraction–expansion coefficient for the multipolar radial exponential parameters, ζ_l.

	PV	*DX*	*DY*	*DZ*	*QZ2*	*QXZ*	*QYZ*	*QX2-Y2*	*QXY*	*OZ3*	*OXZ2*	*OYZ2*	*OX2-Y2*	*OXYZ*	*OX3*	*OY3*
Cα0	4·38 (4)	−0·18 (2)	0·00 (2)	0·03 (2)	0·11 (2)	0·06 (2)	−0·02 (2)	−0·05 (2)	0·03 (2)	0·03 (2)	−0·21 (2)	0·02 (2)	−0·03 (2)	−0·03 (2)	0·24 (2)	−0·00 (2)
C0	4·24 (6)	0·17 (3)	0·02 (3)	−0·05 (2)	−0·36 (2)	−0·01 (3)	0·01 (2)	0·15 (3)	0·09 (3)	−0·03 (3)	0·04 (3)	−0·01 (2)	−0·04 (3)	−0·02 (3)	0·51 (3)	−0·01 (4)
Cα	4·38 (6)	0·06 (3)	−0·03 (3)	0·07 (3)	−0·05 (3)	−0·11 (3)	−0·02 (3)	0·06 (3)	0·04 (3)	0·03 (3)	−0·12 (3)	−0·33 (3)	−0·02 (4)	0·04 (4)	0·28 (3)	0·08 (4)
Cβ	4·30 (7)	−0·06 (3)	0·19 (3)	−0·13 (3)	0·06 (3)	0·04 (3)	−0·02 (3)	0·04 (3)	−0·06 (3)	0·01 (4)	−0·22 (4)	−0·28 (4)	−0·01 (4)	−0·01 (4)	0·20 (4)	0·06 (4)
Cγ	4·37 (8)	0·14 (5)	0·04 (5)	0·01 (3)	−0·33 (3)	0·01 (3)	−0·01 (3)	0·00 (5)	0·06 (4)	−0·07 (4)	0·02 (4)	0·01 (4)	−0·00 (5)	0·08 (5)	0·37 (6)	0·19 (6)
Cδ1	4·04 (9)	−0·05 (3)	−0·00 (3)	−0·08 (2)	−0·19 (3)	0·00 (2)	−0·03 (2)	0·03 (3)	0·06 (3)	0·01 (3)	0·07 (3)	−0·06 (3)	0·01 (3)	0·01 (3)	0·23 (3)	0·05 (3)
Cε2	4·11 (7)	0·13 (6)	0·18 (5)	0·08 (4)	−0·33 (4)	0·09 (4)	−0·05 (4)	0·10 (5)	−0·00 (5)	−0·03 (5)	−0·08 (4)	−0·05 (5)	0·01 (5)	−0·10 (5)	0·48 (6)	−0·29 (6)
Cδ2	3·86 (9)	−0·04 (4)	−0·05 (4)	0·07 (3)	−0·19 (3)	0·02 (3)	−0·01 (3)	0·01 (4)	−0·10 (4)	−0·07 (4)	−0·04 (3)	−0·01 (3)	0·07 (4)	0·03 (4)	0·37 (4)	0·04 (3)
Cε3	4·20 (2)	−0·02 (1)	−0·03 (1)	0·01 (2)	−0·21 (1)	−0·01 (2)	0·01 (1)	0·02 (1)	−0·03 (1)	0·02 (2)	0·02 (1)	0·01 (1)	−0·03 (1)	0·00 (1)	0·29 (1)	0·01 (1)
O0	6·32 (3)	−0·17 (2)	0·05 (2)	0·00 (2)	−0·09 (2)	−0·01 (2)	−0·02 (2)	−0·12 (2)	0·06 (2)	0·00 (2)	−0·07 (2)	0·05 (2)	0·01 (2)	−0·00 (2)	0·02 (2)	−0·04 (2)
N1	5·44 (4)	0·03 (2)	0·10 (2)	−0·02 (2)	−0·15 (2)	0·02 (2)	0·00 (2)	−0·06 (2)	−0·00 (2)	0·00 (2)	−0·02 (2)	0·01 (2)	0·00 (2)	0·04 (2)	0·32 (2)	−0·00 (2)
Nε1	5·33 (6)	−0·07 (3)	0·02 (3)	0·05 (3)	−0·12 (3)	−0·06 (2)	−0·00 (2)	−0·06 (3)	0·09 (3)	−0·09 (3)	0·03 (3)	0·03 (3)	0·04 (3)	0·03 (3)	0·29 (4)	−0·02 (4)
HC	0·73 (1)	0·12 (1)														
HN	0·59 (2)	0·23 (3)														

	κ	κ'		κ	κ'
Cα0	0·995 (3)	0·90 (2) = Cα2	Cδ2	0·997 (4)	0·88 (2)
C0	0·975 (2)	0·84 (1) = C1	Cε3	0·996 (2)	0·92 (2) = Cζ3 = Cη = Cζ2
Cα	0·965 (3)	0·86 (2)	O0	0·975 (1)	0·64 (2) = O1
Cβ	0·986 (4)	0·84 (2)	N1	0·981 (2)	0·78 (2) = N2
Cγ	0·995 (3)	0·80 (2)	Nε1	0·996 (2)	0·78 (3)
Cδ1	1·008 (4)	1·04 (4)	HC	1·076 (6)	1·08 (3) = H − C
Cε2	1·002 (3)	0·71 (1)	HN	1·035 (13)	0·72 (3) = H − N

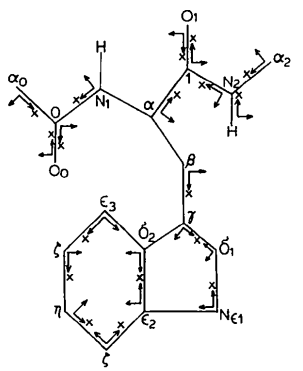

Fig. 2. Directions of local orthogonal reference axes for the atom-centered multiple functions (see Table 4).

Table 5. *Selected valence angles* (°) *and conformation angles* (°)

E.s.d.'s are 0·1° or less.

Cα0—C0—O0	121·6	Cα—Cβ—Cγ	112·0
N1	116·9	Cβ—Cγ—Cδ1	126·9
C0—N1—Cα	121·4	Cδ2	126·8
N1—Cα—Cβ	109·1	Cγ—Cδ1—Nε1	110·4
C1	110·8	Cδ1—Nε1—Cε2	108·7
Cα—C1—O1	122·4	Nε1—Cε2—Cδ2	107·9
N2	113·6	Cζ2	130·0
C1—N2—Cα2	123·3	Cε2—Cζ2—Cη	117·7
		Cζ2—Cη—Cζ3	121·1
		Cη—Cζ3—Cε3	121·2
		Cζ3—Cε3—Cδ2	118·8

ω_0 = Cα0—Co—N1—Cα	= −179·9	ψ_1 = N1—Cα—C1—N2	= 169·0
φ_1 = C0—N1—Cα—C1	= −77·8	ω_1 = Cα—C1—N2—Cα2	= −175·2
χ_1 = N1—Cα—Cβ—Cγ	= −68·0	χ_2 = Cα—Cβ—Cγ—Cδ1	= 93·9

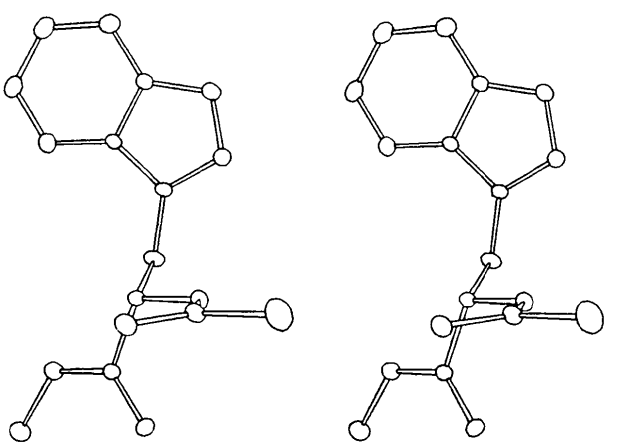

Fig. 3. Molecular conformation and thermal motion. Ellipsoids are shown at 50% probability.

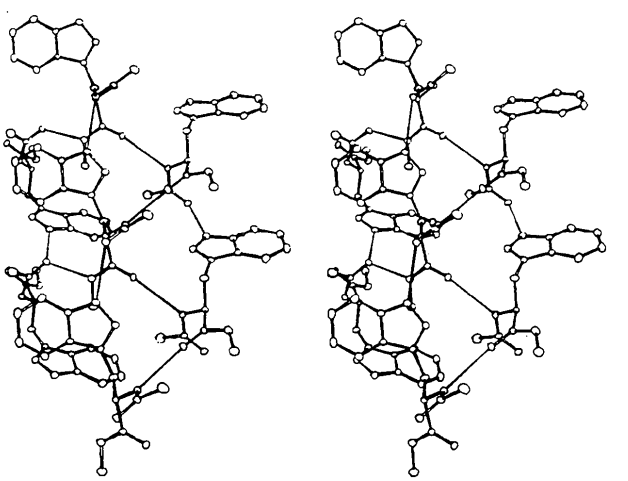

Fig. 4. Crystal packing and hydrogen bonding.

pairs of non-H atoms. The exceptions were $|\Delta| = 0.0019$ and 0.0012 Å^2 for the Cγ—Cδ2 and Cε3—Cζ3 bonds in the indole ring, and $|\Delta| = 0.0015$ and 0.0016 Å for the Cα0—C0 and N2—Cα2 bonds at the two ends of the peptide chain. Along nonbonded intramolecular interatomic directions, some $|\Delta|$ values were considerably larger ($|\Delta|_{max} = 0.014$ Å^2), indicating that the molecule is not entirely rigid and that low-frequency soft modes of internal molecular vibration contribute significantly to the observed mean-square displacements (Rosenfeld, Trueblood & Dunitz, 1978).

The mean-square atomic displacements were modelled by fitting molecular **T**, **L** and **S** plus correlated φ_i tensors to the atomic **U** tensors. The **T**, **L** and **S** model the external lattice vibrations of the whole molecule; the φ_i model low-frequency large-amplitude internal molecular vibrations as librations of rigid groups of atoms within the flexible molecule (Dunitz, Schomaker & Trueblood, 1988; Dunitz, Maverick & Trueblood, 1988). Selected results are summarized in Table 6, which shows that at 100 K the lattice vibrations are damped such that the internal librations contribute as much as or more than the external librations to the total mean-square atomic displacements, roughly half of which are still due to the translational lattice modes.

Various models for the internal librations were tried. The best results were obtained with Cα as a flexible joint linking three librating rigid groups, namely, the Cβ-indole and the two blocked-peptide groups (Table 6). Other models included libration of the indole ring about the Cβ—Cγ bond and a wagging of the indole ring by bending the Cα—Cβ—Cγ valence angle. These models were rejected because they gave significantly negative principal mean-square amplitudes, or they produced only an insignificant improvement over the rigid-molecule statistics of fit.

The model with three-way flexibility at Cα is also indirectly supported by the corresponding DL-racemate crystal structure (Harada & Iitaka, 1977), in which the conformational angles at Cα in the L-molecule ($\varphi 1 = -103.7$, $\psi 1 = 141.4$, $\chi 1 = -65.3°$) differ significantly from the values reported in Table 5. The differences are large ($\sim 30°$) for the two softer torsional modes, which correspond to φ_1 and ψ_1, and the difference is small (3°) for the harder mode, which corresponds to χ_1. Similarly, the conformational angle φ_1, which corresponds to the softest of the torsional modes, changes by 4° between 100 K (Table 5) and 300 K (Souhassou *et al.*, 1990), while ψ_1 and χ_1 change by only 1·1° and 0·9°, respectively. The *TLS* + Φ_i model was also fitted to the U^{jk} from the 300 K crystal structure determination (Souhassou *et al.*, 1990). The principal mean-square amplitudes at 300 K were two or three times larger than the values at 100 K given in Table 6, but the force constants for the three internal torsional modes were, to within the error of fit, constant between the two temperatures.

Table 6. *Statistics of fit, principal mean-square amplitudes, and torsional force constants from the fit of molecular TLS + Φ_i to the atomic U^{jk}*

Statistics of fit: $\chi^2 = \sum w[U^{jk} - U^{jk}(TLS+\Phi_i)]^2$, $w = 1/\sigma^2(U^{jk})$; $R = (\chi^2/\sum wU^{jk\,2})^{1/2}$; $S = [\chi^2/(n-m)]^{1/2}$; n observations U^{jk}; m parameters: six T, six L, and eight S parameters plus six parameters per Φ_i. The six parameters per internal torsional mode are $(\langle\varphi^2\rangle + 2\langle\varphi\lambda_z\rangle)$, $\langle\varphi\lambda_x\rangle$, $\langle\varphi\lambda_y\rangle$, $\langle\varphi t_z\rangle$, $\langle\varphi t_x\rangle$, $\langle\varphi t_y\rangle$, where z designates the direction of the torsional axis, and x and y designate directions perpendicular to it. The quantity listed in the table as $\langle\varphi^2\rangle$ is in fact $(\langle\varphi\rangle^2 + 2\langle\varphi\lambda_z\rangle)$. Although the eigenvalue L_3 is negative, it is only insignificantly so.

	Rigid molecule	Flexible molecule	Whole-molecule Translations $\langle t^2\rangle$ (Å^2)	Whole-molecule Librations $\langle\lambda^2\rangle$ (deg^2)
R	0·21	0·12	T_1 0·0176	L_1 4·38
S	4·20	2·46	T_2 0·0118	L_2 3·70
n	114	114	T_3 0·0096	L_3 −0·26
m	20	38		

Librating group	Libration axis	Torsion angle	$\langle\varphi^2\rangle$ (deg^2)	Force constant (J mol^{-1} deg^{-2})
C0, O0, Cα0 about	Cα—N1	φ_1	25·8	34 (8)
O2, N2, Cα2 about	Cα—C1	ψ_1	20·0	46 (12)
Indole ring about	Cα—Cβ	χ_1	3·1	276 (70)

The *TLS* + Φ_i analyses were carried out using the *THMA*11 program of Trueblood (1990), which includes a six-parameter model for the physical correlations between each internal torsional mode and the external lattice modes. In the cases at hand, modelling these correlations was essential. Ignoring the correlations, and fitting a simpler model (Dunitz & White, 1973; Trueblood, 1978) with just one parameter, rather than six parameters, per internal torsional mode gave no significant improvement over the statistics of fit obtained with the rigid-molecule model.

Electron density maps and the phase problem

The crystallographic deformation density maps were calculated according to

$$\Delta\rho(\mathbf{r}) = V^{-1}\sum_{\mathbf{h}}[|F_m(\mathbf{h})|\exp i\varphi_m(\mathbf{h}) - |F_s(\mathbf{h})|\exp i\varphi_s(\mathbf{h})]\exp(-2\pi i\mathbf{h}.\mathbf{r}) \quad (3)$$

where the subscripts m designate the atom-centered multipolar density model, and s the spherically averaged free-atom superposition model. The summations included the 2739 terms with $(\sin\theta)/\lambda < 0.9$ Å^{-1}.

Equation (3) shows that, with a noncentrosymmetric structure, reliable deformation-density maps require two sets of structure amplitudes *and* two sets of phases. A conventional $\Delta|F|$ synthesis,

$$\Delta\rho = V^{-1}\sum(k^{-1}|F_o| - |F_c|)\exp(i\varphi_c) \times \exp(-2\pi i\mathbf{h}.\mathbf{r}), \quad (4)$$

cannot be properly phased by a spherical-atom model alone, even if unbiased structural parameters

are derived from a high-angle X-ray refinement or from neutron data (Coppens, 1974). The effect of the phase differences $\Delta\varphi = \varphi_m - \varphi_s$ is calculated explicitly in *Appendix B*, which shows that the deformation density can be written as the sum of an amplitude-difference density and a phase-difference density.

$$\Delta\rho = \Delta\rho(\Delta|F|) + \Delta\rho(\Delta\varphi), \tag{5}$$

where

$$\Delta\rho(\Delta|F|) = V^{-1}\Sigma(|F_m| - |F_s|)\exp(i\varphi_m) \times \exp(-2\pi i\mathbf{h}.\mathbf{r}) \tag{6}$$

and

$$\Delta\rho(\Delta\varphi) = V^{-1}\Sigma 2|F_s|\sin(\Delta\varphi/2)\exp[i(\varphi_s + \varphi_m + \pi)/2]\exp(-2\pi i\mathbf{h}.\mathbf{r}). \tag{7}$$

The amplitudes of the Fourier components of $\Delta\rho(\Delta\varphi)$ are $2|F_s|\sin(\Delta\varphi/2)$, which for small $\Delta\varphi$ reduce to $|F_s|\Delta\varphi$, and the phases are the average of φ_s and φ_m plus a phase advance of $\pi/2$.

For centrosymmetric structures the phases are restricted to values of 0 or π, and there will be at most a few reflections with very small $|F|$ for which φ_m and φ_s are different; thus, phase differences will make a negligible contribution to the total $\Delta\rho$. In noncentrosymmetric structures, other things being equal, the higher the point-group symmetry the smaller the contribution from the phase differences. For example, the contribution will be smaller in point group 222-C_{2h} (with centric $hk0$, $h0l$ and $0kl$ reflections) than in point group 2-C_2 (with only $h0l$ centric reflections). On the other hand, glide-plane space-group symmetry might extinguish half the reflections in a centric zone, and thereby increase the relative contribution of the phase differences.

Fig. 5 shows maps of the total $\Delta\rho$ and $\Delta\rho(\Delta\varphi)$ for the indole ring. The $\Delta\rho$ map was calculated with $|F_m|$ in equation (3) replaced by $k^{-1}|F_o|$, so that random experimental errors are also expressed in the $\Delta\rho$ map. The maximum $\Delta\rho(\Delta\varphi)$ is 0·14 e Å^{-3} along the Cζ3—Cη bond. The average $\Delta\rho(\Delta\varphi)$ peak height is 0·08 e Å^{-3}, and although this is less than $2\langle\sigma^2(\Delta\rho)\rangle^{1/2}$ the pattern of the $\Delta\rho(\Delta\varphi)$ density is clearly significant. Because the $hk0$, $h0l$, and $0kl$ zones are centric, $\Delta\rho(\Delta\varphi)$ is much smaller than that observed in a preliminary study (Souhassou, Lecomte & Aubry, 1988) of *N*-acetyl-α,β-dehydrophenylalanine methylamide, which crystallizes in space group *Cc* (point group *m*-C_s, only $0k0$ centric) and which had maximum and average values of 0·23 and 0·19 e Å^{-3} for $\Delta\rho(\Delta\varphi)$ peak heights around the phenyl ring.

As Fig. 5(*b*) illustrates, phase errors tend to flatten the difference electron densities mapped for noncentrosymmetric structures. These effects have been noted also by Klein, Majeste & Stevens (1987) and by Savariault & Lehmann (1980), who estimated that for a structure with no symmetry-restricted phases the maximum effect of a uniform random distribution of phase errors would be to reduce the difference density by a factor of one-half.

Fig. 6 shows the distribution of $|F|\Delta\varphi$ as a function of $(\sin\theta)/\lambda$ and of $|F|$. Predictably, owing to the diffuseness of the valence-electron distribution, $|F|\Delta\varphi$ tends to increase with decreasing $(\sin\theta)/\lambda$ (Fig. 6*a*). It is also apparent (Fig. 6*b*) that the weak and medium-weak reflections have an important influence. Consequently, the measurement and the processing of the low-angle weak reflections deserve special care.

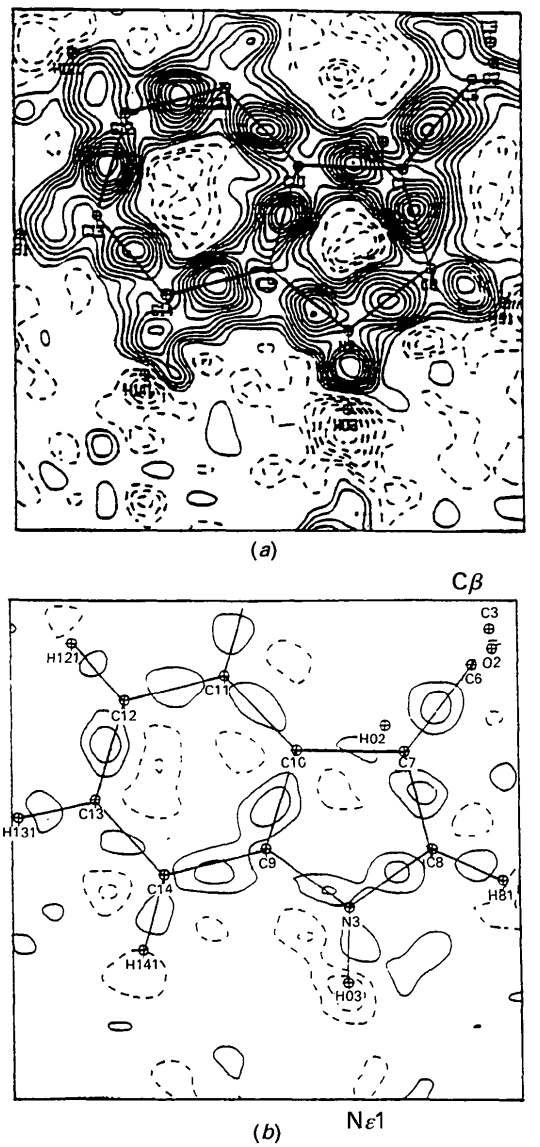

Fig. 5. Maps of (*a*) the total experimental $\Delta\rho$ and (*b*) $\Delta\rho(\Delta\varphi)$ in the plane of the indole ring. Contours as in Fig. 1.

Quantum-chemical calculations

Ab initio self-consistent-field molecular-orbital calculations were carried out on *N*-Ac-L-Trp-NHMe using the crystallographic molecular geometry and basis sets (Huzinaga, 1971) composed of 524 primitive Gaussian functions, (9*s*5*p*) for C, N and O and (4*s*) for H, contracted to 205 split-valence Gaussian-type orbitals, [3*s*2*p*] and [2*s*], respectively.

The total energy associated with the molecular wave function is −852·2807 h. The two highest-energy occupied orbitals, at −0·30 and −0·33 h, are π-bonding combinations delocalized over the indole ring. Just below these, three orbitals are clustered at −0·39 h. Two of them can be described as nonbonding π orbitals localized over the N and O atoms of the peptide groups, and the third belongs to the indole π system. The lowest-energy unoccupied orbital, at +0·09 h, is a π^* antibonding orbital, delocalized mainly over the Cγ—Cδ1, Cδ2—Cε3 and Cζ2—Cη bonds of the indole ring.

The wave function of the promolecule was computed as the orthonormalized superposition of atomic wave functions obtained with the same basis sets, at the same level of calculation. The deformation-density distribution was obtained in the planes of interest as the difference between the electron densities from the two wave functions,

$$\Delta\rho(x,y,z) = \rho_{\mathrm{MOL}}(x,y,z) - \rho_{\mathrm{PROMOL}}(x,y,z).$$

The quantum-chemical calculations were carried out using the *ASTERIX* program system vectorized for CRAY-2 computers (Ernenwein, Rohmer & Bénard, 1990; Rohmer, Demuynck, Bénard, Wiest, Bachmann, Henriet & Ernenwein, 1990).

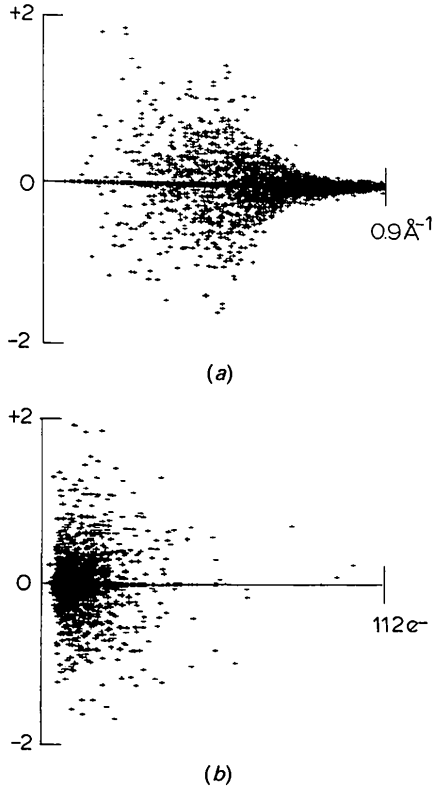

Fig. 6. Distribution of $|F|\Delta\varphi$ (in units of electrons) against (*a*) $(\sin\theta)/\lambda$ and (*b*) $|F|$.

Discussion

The experimental crystallographic density maps are limited to a resolution corresponding to $d_{\min} = \lambda/(2\sin\theta_{\max}) = 0{\cdot}56$ Å, and they are dynamic maps showing the electron distribution averaged over the experimentally observed thermal motion. The theoretical, quantum-chemical maps show a static, free-molecule electron distribution at infinite resolution. Hence, the generally good absolute agreement between the experimental and theoretical bond-density peak heights is somewhat accidental: the effects of the omission of polarization functions from the theoretical basis set roughly balance the effects of thermal smearing and finite resolution on the experimental density. What is more significant, however, is that both experiment and theory show much the same relative trends from bond to bond.

The H *atoms*

In the experimental maps, there are −0·2 to −0·4 e Å^{-3} minima near the H atoms, opposite the C—H and N—H bond maxima, but there are no such minima in the theoretical maps. Some small part of the differences between experiment and theory arise because the spherically contracted bound H atom (Stewart *et al.*, 1965) was subtracted for the crystallographic maps, while the uncontracted free atom was subtracted for the quantum-chemical maps. A larger part of the differences probably arises as an artifact of the experimental H-atom modelling. The H atoms were positioned to give 1·07 Å C—H and 1·03 Å N—H bond lengths. Any error in the hydrogen positions will produce strongly correlated errors in the hydrogen dipole populations. These correlations are probably largely responsible for the experimental minima near the H atoms, which may indicate that the chosen C—H and N—H bond lengths were a little too long. In addition, there are strong correlations between the refined monopole populations and mean-square atomic displacements for the H atoms, and these, in turn, bias the valence-shell population parameters.

The indole ring

Fig. 7 gives the experimental and theoretical deformation maps for the Cβ-indole group. Except for a

slight polarization of the Cε2—N bond density toward N in the experimental map, the density maxima are centered along the bonds in both maps. Both maps show the C—N peaks to be ~0·10 e Å^{-3} lower than the C—C peaks. This is because spherically averaged atoms are the reference state subtracted for the deformation densities. A spherically averaged N atom has $\frac{5}{4}$ electrons per *L*-shell orbital, while an *sp*-, *sp*^{2}-, or *sp*^{3}-hybridized N atom has one electron in each of three bonding orbitals and one pair of electrons in a nonbonding orbital. Analogous descriptions apply to spherically averaged O and F atoms with, respectively, $\frac{6}{4}$ and $\frac{7}{4}$ electrons per *L*-shell orbital. By contrast, a C atom has one electron per *L*-shell orbital, whether spherically averaged or *s* and *p* hybridized. The effect of subtraction of spherically averaged N, O and F atoms, leading to apparently deficient bond-pair densities, and, by corollary, excessive lone-pair densities, has been well documented in both experimental and theoretical studies (Dunitz & Seiler, 1983; Kunze & Hall, 1986).

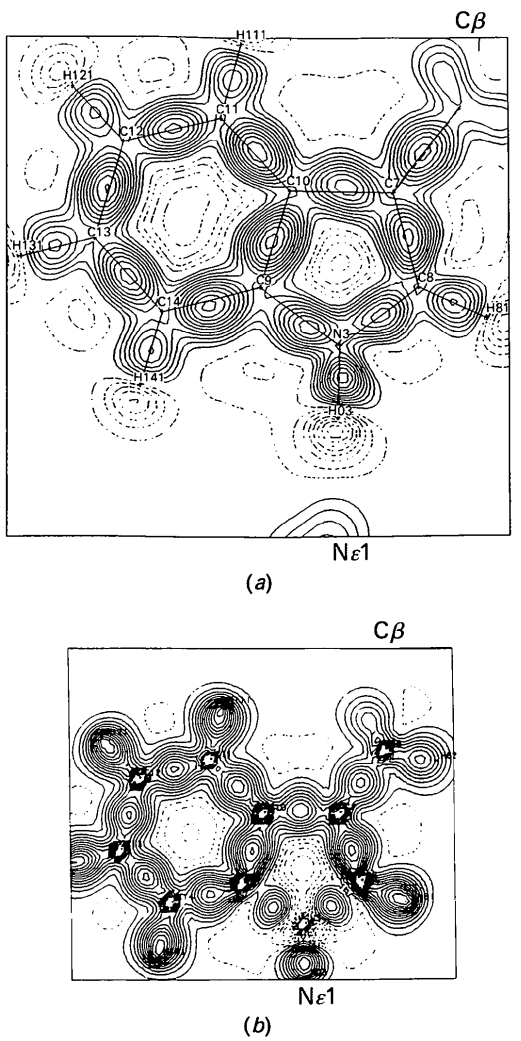

Fig. 7. (*a*) Crystallographic dynamic and (*b*) quantum-chemical static deformation-density maps in the plane of the Cβ-indole group. Contours as in Fig. 1.

Table 7. *Deformation-density peak heights* (e Å^{-3}) *and bond lengths* (Å)

Bond length e.s.d.'s average 0·0015 Å.

	Theory	Experiment	
Indole ring			
Cβ—Cγ	0·40	0·50	1·498
Cγ—Cδ1	0·55	0·50	1·368
Cδ1—Nε1	0·30	0·40	1·374
Nε1—Cε2	0·30	0·45	1·371
Cε2—Cδ2	0·55	0·55	1·414
Cδ2—Cε3	0·50	0·50	1·405
Cε3—Cζ3	0·50	0·45	1·383
Cζ3—Cη	0·50	0·55	1·410
Cη—Cζ2	0·50	0·45	1·379
Cζ2—Cε2	0·50	0·55	1·398
Peptide groups			
Cα0—C0	0·45	0·40	1·496
C0—O0	0·40	0·50	1·248
C0—N1	0·40	0·60	1·334
N1—Cα	0·25	0·45	1·448
Cα—C1	0·45	0·50	1·541
C1—O1	0·40	0·50	1·232
C1—N2	0·35	0·60	1·338
N2—Cα2	0·25	0·40	1·450
Lone pairs			
O0	1·30	0·25	
O1	1·30	0·25	

Table 7 compares the peak heights in relation to the bond lengths. The theoretical peak heights follow the bond-length alternation in the five-membered ring of the indole, with higher peaks for the shorter Cγ—Cδ1 and Cδ2—Cε2 bonds, but the experimental peak heights are more uniform.

Close to the indole N atom the theoretical map shows three −0·25 e Å^{-3} density minima, which do not appear on the experimental map, and the theoretical C—N bond peaks are about one-third lower than the experimental. Similar differences are seen for the peptide C—N densities, and these differences are discussed below.

The peptide groups

The experimental density maps for the peptide groups are shown in Fig. 8, and the corresponding theoretical maps in Fig. 9. Both theory and experiment confirm the chemical equivalence of the N- and C-terminal peptide groups. They are effectively isolated from electronic conjugation with each other or with the indole ring by the aliphatic C(α)H—C(β)H$_2$ group.

The main differences between the theoretical and experimental maps are that the C—N bond peaks are roughly one third lower in the theoretical map, and the experimental map does not show a trigonal electron depopulation close to the N atoms. These differences are attributable to the absence of *d*-type polarization functions in the theoretical basis set and to the experimental thermal smearing.

Deformation densities from extended basis set calculations including polarization functions for formamide (Stevens, Rys & Coppens, 1978) and for urea (Swaminathan, Craven, Spackman & Stewart, 1984) showed C—N bond peaks of 0·60 e Å^{-3} centered along the bonds. By contrast, a calculation for urea with a less flexible split-valence basis set, comparable to our basis set, gave a C—N peak of only 0·34 e Å^{-3} (Scheringer, Mullen, Hellner, Hase, Schulte & Schweig, 1978). For both urea and formamide, the static density minima of about −0·3 e Å^{-3} close to the N atoms were obliterated when thermal smearing was applied and dynamic density maps were computed. The same dependencies on basis set and thermal smearing were confirmed in calculations for urea, imidazolidone, and glycoluril (Moss, Blessing & DeTitta, 1985).

All these quantum-chemical studies of amide molecules also showed that the C—O density and the O-atom lone-pair densities are affected much less than the C—N density by the omission of polarization functions. The lone-pair densities are, however, very much affected by thermal smearing, which decreased the peak heights from 1·2 to 0·5 e Å^{-3} for urea (Scheringer *et al.*, 1978), and from 1·2 to 0·4 e Å^{-3} for formamide (Stevens *et al.*, 1978). The lone-pair peaks are 1·3 e Å^{-3} on our static theoretical maps, and 0·25 e Å^{-3} on our dynamic experi-

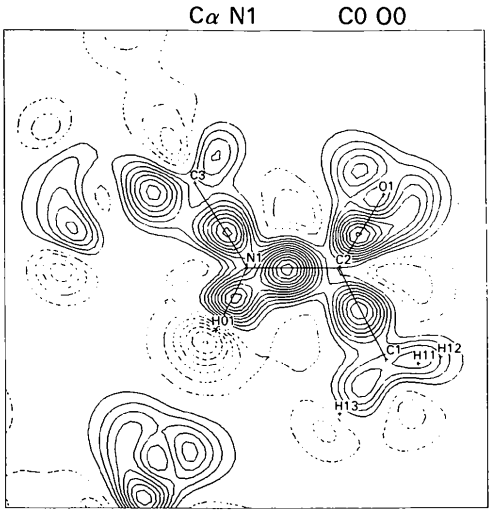

(*a*)

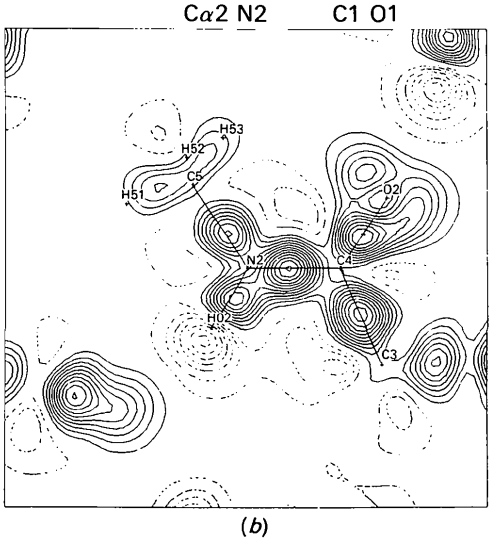

(*b*)

Fig. 8. Crystallographic deformation-density maps in the planes of (*a*) the N-terminal and (*b*) the C-terminal peptide groups. Contours as in Fig. 1.

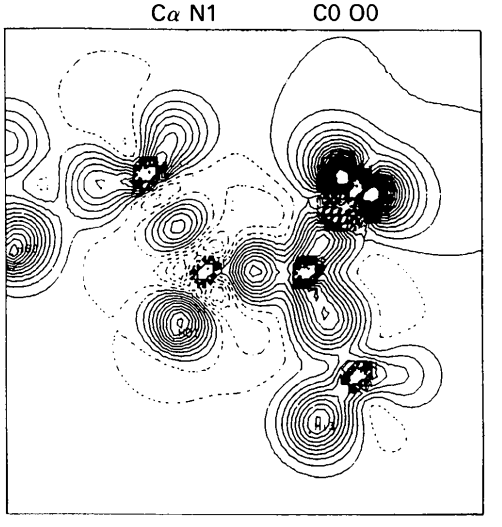

(*a*)

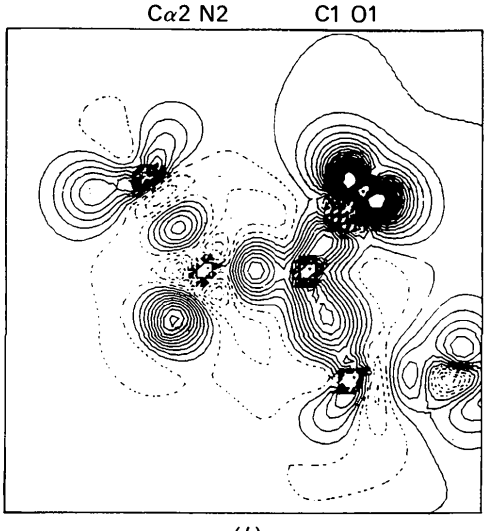

(*b*)

Fig. 9. Quantum-chemical deformation-density maps in the planes of (*a*) the N-terminal and (*b*) the C-terminal peptide groups. Contours as in Fig. 1.

mental maps. The decrease is larger in our case because the thermal motion is larger than in the formamide and urea crystals. The lone-pair peaks are very sensitive to thermal smearing because they are sharp peaks very close to the nucleus.

The different π character in the shorter N—C(O) and longer N—Cα bonds along the peptide chain is evident in both the experimental and theoretical densities (Table 7 and Figs. 10 and 11). In both sets of maps, the bond-density maxima are higher for the shorter bonds [(*a*) and (*c*) in Figs. 10 and 11]. In the planes perpendicular to the N(H)—C—O amide planes, the C-atom densities are depleted, and the N-atom densities are slightly polarized toward the C atoms. These features are consistent with the idea of π-bond donation from N to C to O, *i.e.* —N(H)—C(=O)— $\leftrightarrow$ —N^+(H)=C(O^-)—. Neither set of maps shows any evidence of π bonding in the N—Cα bonds, and the theoretical maps (Fig. 11) indicate that the N $p\pi$ density remains localized mainly in a nonbonding orbital. This nonbonding $p\pi$ density is to some extent an artifact due to the subtraction of a spherically averaged N atom, as discussed above, but it is also consistent with the molecular-orbital Mulliken population analysis.

The π system of each N(H)—C—O peptide group has two doubly occupied molecular orbitals, each of them quasi-degenerate with its equivalent in the

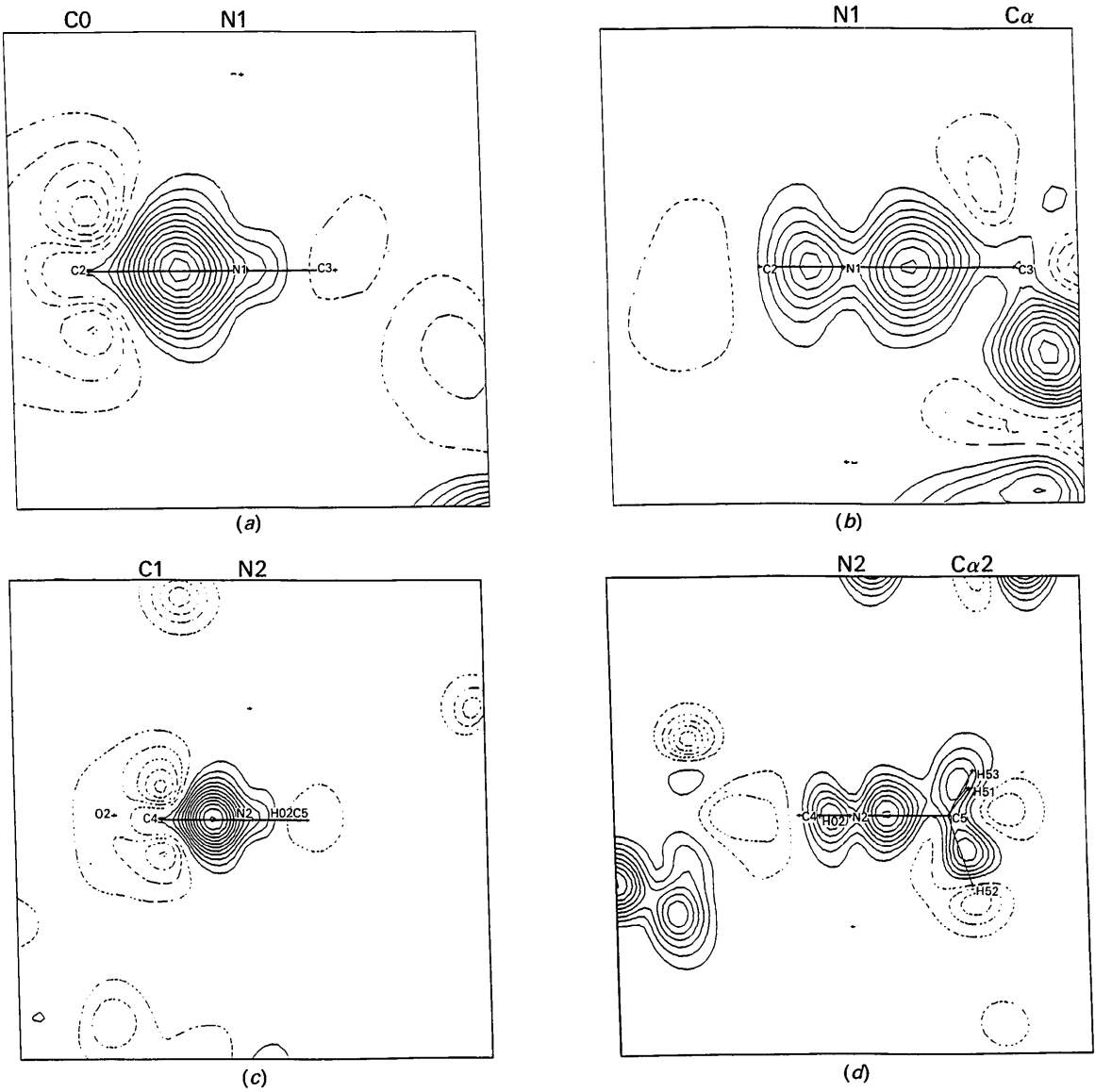

Fig. 10. Crystallographic deformation densities in the planes perpendicular to the N(H)—C—O peptide planes: (*a*) C0—N1, (*b*) N1—Cα, (*c*) C1—N2, and (*d*) N2—Cα2. Contours as in Fig. 1.

other peptide group. The lower-energy orbital (−0·50 h) is bonding and fully delocalized over the N, C and O atoms. The higher-energy orbital (−0·39 h) is localized on N and O and is therefore nonbonding. The population analysis consistently assigns high populations to the π orbitals of N and O (1·81 and 1·53 e for N1 and O0; 1·69 and 1·48 e for N2 and O1), and low populations to the peptide C atoms (0·69 e for C0, 0·72 e for C1).

The π-nonbonding densities of the N atoms are not so apparent in the experimental maps (Fig. 10). For the longer N—Cα bonds, Figs. 10(*b*) and 10(*d*) show substantial accumulations of density distinct from the N—Cα bond peaks, but the resolution is not sufficient to show separate π lobes. For the shorter N—C(O) bonds, Figs. 10(*a*) and 10(*c*) show an extension of the N—C bond peak toward and beyond the N atom, but not a second resolved peak. The experimental results do, however, agree very well with the results obtained by Eisenstein (1988) for cytosine and adenine and with our preliminary results for *N*-acetyl-α,β-dehydrophenylalanine methylamide (Souhassou, *et al.*, 1988). Thus the differences between the experimental and theoretical nonbonding π-N densities in our present work are, again, probably due to the omission of polarization functions from the theoretical basis set.

The hydrogen bonds

Fig. 12 shows the experimental deformation density in the planes of the hydrogen bonds, all of which are intermolecular. The O1 atom accepts a single hydrogen bond, N1—H···O, N···O 3·01 Å. Fig. 12(*a*) shows that the two O1 lone pairs are located in the plane of the hydrogen bond, and that the N1—H bond is directed between the two rather than towards one of them. A significant −0·30 e Å^{-3} density minimum occurs close to the H atom, between it and O1. Although this is consistent with an electrostatic description of hydrogen bonding, similar minima also occur on the experimental maps for the other H atoms not involved in hydrogen bonding, and corresponding minima do not occur on the theoretical maps. As discussed above, these differences may be due in large part to artifacts of the hydrogen modelling in the experimental analysis.

Fig. 12(*b*) shows that O0 accepts two hydrogen bonds, N2—H···O···H—Nε3, N2···O 2·88, Nε3···O

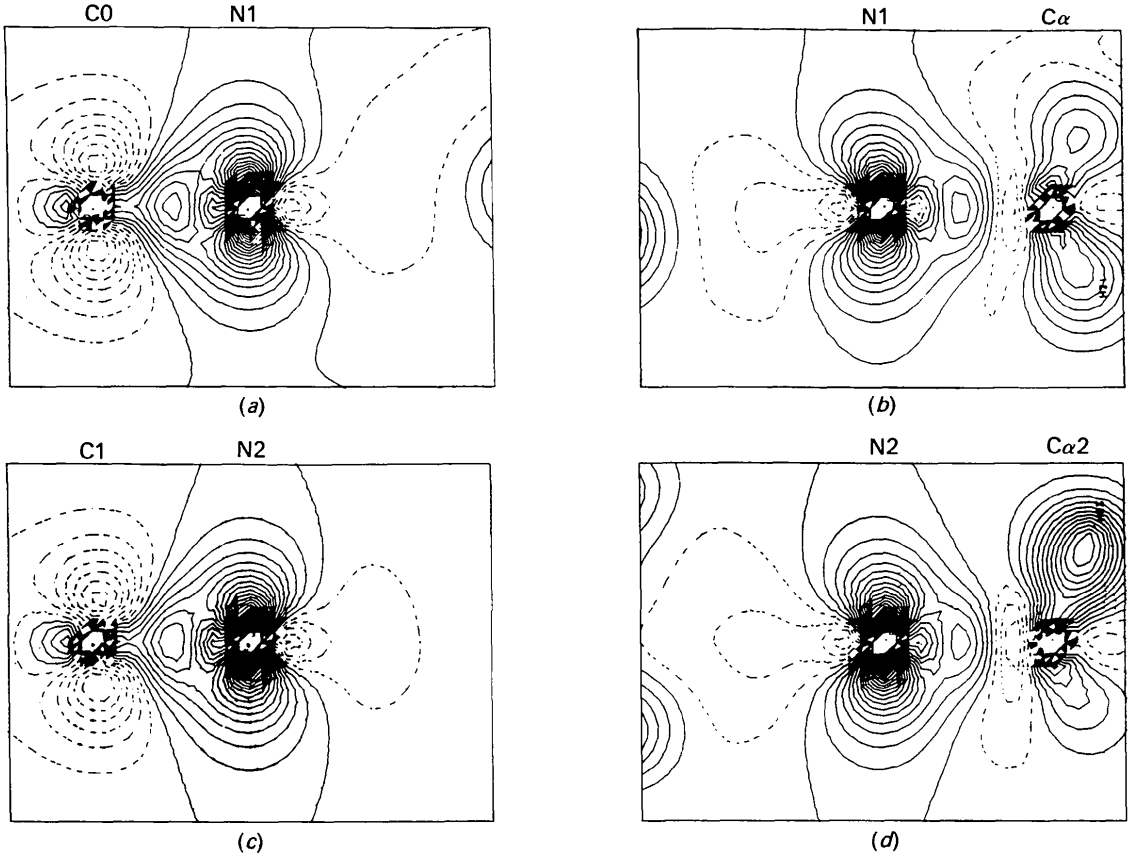

Fig. 11. Quantum-chemical deformation densities in the planes perpendicular to the N(H)—C—O peptide planes: (*a*) C0—N1, (*b*) N1—Cα, (*c*) C1—N2, and (*d*) N2—Cα2. Contours as in Fig. 1.

2·89 Å, and H···O···H 122·6°. These hydrogen bonds lie in a plane approximately perpendicular to the plane of the O0 lone pairs, which is an exception to the usual coplanar arrangement as seen, for example, in crystals of formamide (Stevens *et al.*, 1978) and thiourea–parabanic acid (Weber & Craven, 1987).

Concluding remarks

Experiment and theory yield deformation-density maps for *N*-Ac-L-Trp-NHMe that are consistent with chemical bonding concepts of C—C bond strength *versus* bond length and partial double-bond character in the N(H)—C(O) *trans*-amide bond of peptides. Within the limitations imposed by the split-valence-basis quantum-chemical approximations and the crystallographic thermal-motion convolution and finite resolution, reasonable quantitative agreement is obtained. More detailed comparison requires polarization functions in the theoretical basis set and high-resolution static density maps from the experimental data. Further work on the molecular electrostatic potential is in progress.

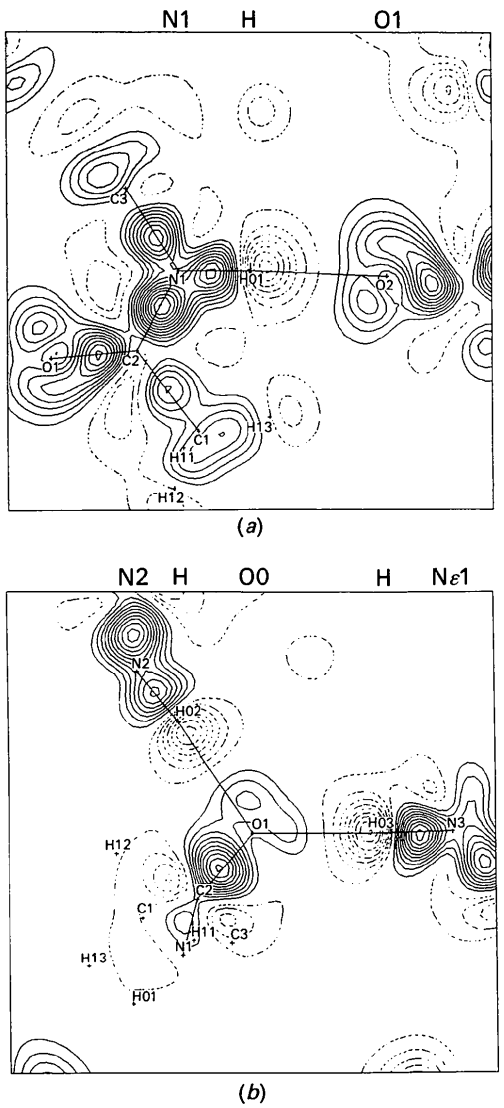

Fig. 12. Crystallographic deformation in the planes of the hydrogen bonds: (*a*) N1—H···O1 and (*b*) N2—H ···O0···H—Nε1. Contours as in Fig. 1.

The quantum-chemical calculations were carried out with a grant of CRAY-2 computer time from the Conseil Scientifique du Centre de Calcul Vectoriel de la Recherche (Palaiseau, France). AA, MM and CL are grateful for support from CEE grant No. ST2J-0184. RHB is grateful for the hospitality of the Laboratoire de Cristallographie de l'Université de Nancy I during a three-month visiting professorship, and for support from USDHHS PHS NIH grants No. GM34073 and DK19856. We thank Professor K. N. Trueblood for providing a copy of his program *THMA*11.

APPENDIX A

Goodness-of-fit after refinement against averaged data

When the equivalent data, $y_i = |F|_i^2$, were averaged,

$$y = \sum_i w_i y_i / \sum_i w_i, \quad i = 1,2,...,n, \quad w_i = 1/\sigma^2(y_i), \qquad (A.1)$$

two measures of the experimental error were calculated,

$$\sigma^2_{\text{int}} = [n/(n-1)]\sum_i w_i (y_i - y)^2 / \sum_i w_i \qquad (A.2)$$

and

$$\sigma^2_{\text{ext}} = \sum_i w_i \sigma^2(y_i) / \sum_i w_i = n / \sum_i w_i, \qquad (A.3)$$

and an analysis of variance based on the ratios

$$\sigma_{\text{int}} / \sigma_{\text{ext}} = r[y, (\sin\theta)/\lambda] \qquad (A.4)$$

was carried out to obtain adjusted error estimates $\sigma(y) = r\sigma_{\text{ext}}$ and to calculate weights $w = 1/\sigma^2(y)$ for the least-squares refinements.

The presence of the factor n in the numerators of the two expressions (*A*.2 and *A*.3) for σ^2 means that the σ^2 values estimate the variance of the population of possible y_i values, not the variance of the estimated mean y. If the n values y_i were uncorrelated independent measurements, then the estimated variance of the sample mean y would be σ^2/n. We expect, however, that the y_i do have correlated errors, although the degree of correlation is unknown, and we therefore use the estimated population variances, rather than estimated variances of the means, to calculate the weights for the least-squares refinements (Blessing, 1987, pp. 44–46).

If n is the average number of measurements per unique datum, then, on average, the variance estimates will be too large by some factor $1 < f < n$, the

weights will be too small by $1/f$, and the goodness of fit $S = [\sum w\Delta^2/(N - M)]^{1/2}$ at the end of the least-squares refinement should ideally approach $1/\sqrt{f}$ rather than unity.

APPENDIX B

The phase problem for deformation densities by Fourier synthesis

The Fourier summation for the model deformation electron density is given by equation (3). Let $\Delta|F| = |F_m| - |F_s|$, then equation (3) can be rewritten as

$$\Delta\rho = V^{-1}\sum[(\Delta|F| + |F_s|)\exp(i\varphi_m) - |F_s|\exp(i\varphi_s)]\exp(-2\pi i\mathbf{h}.\mathbf{r}) \quad (B.1)$$

$$= V^{-1}\sum\Delta|F|\exp(i\varphi_m)\exp(-2\pi i\mathbf{h}.\mathbf{r}) + V^{-1}\sum|F_s|[\exp(i\varphi_m) - \exp(i\varphi_s)]\exp(-2\pi i\mathbf{h}.\mathbf{r}), \quad (B.2)$$

$$\Delta\rho = \Delta\rho(\Delta|F|) + \Delta\rho(\Delta\varphi). \quad (B.3)$$

These results are quoted in equations (5)–(7). Let $\Delta\varphi = \varphi_m - \varphi_s$, then the phase-factor difference, in square brackets, in equation (*B*.2) can be rewritten as follows:

$$\begin{aligned}
\exp(i\varphi_m) - \exp(i\varphi_s) &= \exp[i(\varphi_s + \Delta\varphi)] - \exp(i\varphi_s)\\
&= \exp(i\varphi_s)[\exp(i\Delta\varphi) - 1]\\
&= \exp(i\varphi_s)\exp(i\Delta\varphi/2)\\
&\quad \times [\exp(i\Delta\varphi/2) - \exp(-i\Delta\varphi/2)]\\
&= \exp[i(\varphi_s + \Delta\varphi/2)][2i\sin(\Delta\varphi/2)]\\
&= \exp[i(\varphi_s + \Delta\varphi/2)]\\
&\quad \times [2\exp(i\pi/2)\sin(\Delta\varphi/2)]\\
&= 2\sin(\Delta\varphi/2)\exp[i(\varphi_s\\
&\quad + \Delta\varphi/2 + \pi/2)]\\
&= 2\sin(\Delta\varphi/2)\exp[i(\varphi_s + \varphi_m\\
&\quad + \pi)/2]. \quad (B.4)
\end{aligned}$$

Substitution from (*B*.4) into (*B*.2) gives equation (7).

References

ALLEN, F. (1986). *Acta Cryst.* B**42**, 515–522.

BLESSING, R. H. (1987). *Crystallogr. Rev.* **1**, 3–58.

BLESSING, R. H. (1989). *J. Appl. Cryst.* **22**, 396–397, and references cited therein.

CLEMENTI, E. & RAIMONDI, D. L. (1963). *J. Chem. Phys.* **38**, 2686–2689.

COPPENS, P. (1974). *Acta Cryst.* B**30**, 255–261.

COPPENS, P. (1977). *Isr. J. Chem.* **16**(2,3) 159–162.

CROMER, D. T. (1974). *International Tables for X-ray Crystallography*, Vol. IV, edited by J. A. IBERS & W. C. HAMILTON, pp. 148–151. Birmingham: Kynoch Press. (Present distributor Kluwer Academic Publishers, Dordrecht.)

CRUICKSHANK, D. W. J. (1949). *Acta Cryst.* **2**, 65–82.

DUNITZ, J. D., MAVERICK, E. F. & TRUEBLOOD, K. N. (1988). *Angew. Chem. Int. Ed. Engl.* **27**, 880–895.

DUNITZ, J. D., SCHOMAKER, V. & TRUEBLOOD, K. N. (1988). *J. Phys. Chem.* **92**, 856–867.

DUNITZ, J. D. & SEILER, P. J. (1983). *J. Am. Chem. Soc.* **105**, 7056–7058.

DUNITZ, J. D. & WHITE, D. N. J. (1973). *Acta Cryst.* A**29**, 93–94.

EISENSTEIN, M. (1988). *Acta Cryst.* B**44**, 412–421.

ERNENWEIN, R., ROHMER, M.-M. & BÉNARD, M. (1990). *Comput. Phys. Commun.* **58**, 305–328.

HANSEN, N. & COPPENS, P. (1978). *Acta Cryst.* A**34**, 909–921.

HARADA, Y. & IITAKA, Y. (1977). *Acta Cryst.* B**33**, 244–247.

HIRSHFELD, F. L. (1976). *Acta Cryst.* A**32**, 239–244.

HUZINAGA, S. (1971). *Approximate Atomic Functions*. Technical Report. Univ. of Alberta, Edmonton, Alberta, Canada.

KLEIN, C. L., MAJESTE, R. J. & STEVENS, E. D. (1987). *J. Am. Chem. Soc.* **109**, 6675–6681.

KUNZE, K. L. & HALL, M. B. (1986). *J. Am. Chem. Soc.* **108**, 5122–5127.

MOSS, G. M., BLESSING, R. H. & DETITTA, G. T. (1985). Unpublished results.

ROHMER, M. M., DEMUYNCK, J., BÉNARD, M., WIEST, R., BACHMANN, C., HENRIET, C. & ERNENWEIN, R. (1990). *Comput. Phys. Commun.* **60**, 127–144.

ROSENFELD, R. E. JR, TRUEBLOOD, K. N. & DUNITZ, J. D. (1978). *Acta Cryst.* A**34**, 828–829.

SAVARIAULT, J.-M. & LEHMANN, M. S. (1980). *J. Am. Chem. Soc.* **102**, 1298–1303.

SCHERINGER, C., MULLEN, D., HELLNER, E., HASE, H. L., SCHULTE, K. W. & SCHWEIG, A. (1978). *Acta Cryst.* B**34**, 2241–2243.

SOUHASSOU, M., AUBRY, A., LECOMTE, C. & MARRAUD, M. (1990). *Acta Cryst.* C**46**, 1303–1305.

SOUHASSOU, M., LECOMTE, C. & AUBRY, A. (1988). 2nd Forum on Peptides, Nancy, France. Published as *Colloque Inserm*, Vol. 174, edited by A. AUBRY, M. MARRAUD & B. VITOUX, pp. 359–362. London: John Libbey.

STEVENS, E. D., RYS, J. & COPPENS, P. (1978). *J. Am. Chem. Soc.* **100**, 2324–2329.

STEWART, R. F., DAVIDSON, E. R. & SIMPSON, W. T. (1965). *J. Chem. Phys.* **43**(3), 175–187.

SWAMINATHAN, S., CRAVEN, B. M., SPACKMAN, M. A. & STEWART, R. F. (1984). *Acta Cryst.* B**40**, 398–404.

TRUEBLOOD, K. N. (1978). *Acta Cryst.* A**34**, 950–954.

TRUEBLOOD, K. N. (1990). *THMA*11. Univ. of California at Los Angeles, USA.

WEBER, H.-P. & CRAVEN, B. M. (1987). *Acta Cryst.* B**43**, 202–209.